

# The feasibility of using distributed acoustic sensors in surface seismic application

Samir F. Jreij, Whitney J. Trainor-Guitton, and James L. Simmons

## Colorado School of Mines,

1500 Illinois Ave,

Golden, CO, 80401

(May 1, 2018)

Running head: The feasibility of using distributed acoustic sensors in surface seismic  
application

## ABSTRACT

9 In this paper, an imaging technique that utilizes both multi-component geophones and a surface  
10 distributed acoustic sensor (DAS) acquisition is proposed. The objective of these experiments are  
11 to analyze if the densely sampled DAS fiber data can help improve the image produced by the  
12 sparsely sampled geophones. The PoroTomo survey at Brady's Natural Lab consisted of 238 multi-  
13 component geophones that are spaced anywhere from 60 to 150 meters apart. This proves to be a  
14 difficult migration problem with such sparse spacing. This paper focuses on identifying a method-  
15 ology to resolve the spatial sampling issue. Fortunately, the PoroTomo survey consisted of surface  
16 DAS cable with a 1-meter receiver spacing along the fiber. Both 2D and 3D numerical experiments  
17 are performed to test the feasibility of using the broadside sensitive multi-component geophones  
18 and the densely sampled DAS data together to minimize insensitivity to certain waves. In 2D, a re-  
19 flectivity model is created from the local fault model in the PoroTomo Survey. Quantitative analysis  
20 is performed to provide an unbiased comparison of the results. The quantitative analysis utilized a

21 convolutional neural network to prove that DAS adds value to imaging efforts. A more challenging  
22 example is performed in 3D to confirm the conclusions made in 2D. A methodology to model DAS  
23 data in 3D is presented. The results from quantitative analysis show that utilizing DAS in surface  
24 surveys with sparse, multi-component geophones proves to be useful in improving the classification  
25 accuracy of the image. The results, however, were inconclusive because the migrated images were  
26 too low of a frequency to analyze due to the limitation of the velocity model. Lessons learned from  
27 the data collected at the PoroTomo survey and the numerical experiments are that a more regular  
28 acquisition geometry of the horizontal DAS fiber increases identifying the true reflectors.

## INTRODUCTION

29 Distributed acoustic sensing (DAS) is a technology that uses Rayleigh scattering in a fiber-optic  
30 cable to detect elastic signals when wave particle motion is parallel to the sensing fiber (Hornman  
31 et al., 2013). The two main components used in distributed sensing are the interrogator unit and the  
32 fiber-optic cable. The interrogator unit works as a light source and receiver. It sends a known pulse  
33 of light down the fiber. Nearly any type of existing fiber-optic cable can be used in conjunction  
34 with an interrogator unit. Small imperfections within the fiber cause backscattering of light. Strain  
35 events along the fiber cause this backscattering to change slightly when a wavefield approaches the  
36 fiber. The interrogator unit can measure the Rayleigh backscattering and relate it to the strain along  
37 the fiber.

### 38 **DAS Advantages**

39 DAS has many advantages in various industries. For one, DAS is a low-cost acquisition system  
40 in wells that already contain fiber optic cables. Even in those wells that do not already contain  
41 fiber optic cables, a DAS vertical seismic profile (VSP) is often more affordable than renting and  
42 deploying geophones (Mateeva et al., 2014). DAS also enables seismic surveys to be acquired with  
43 dense sampling (as small as 10-centimeter receiver spacing) at long cable lengths (tens of kilometers  
44 long). Achieving even 1-meter sampling with conventional geophone is expensive and logistically  
45 difficult. Lastly, DAS has almost perfect repeatability in 4-D surveys when cemented in a borehole,  
46 attached to casing, or trenched in the subsurface (Mateeva et al., 2013).

<sup>47</sup> **DAS Disadvantages**

<sup>48</sup> Although DAS may seem like the solution to seismic acquisition, it also has many disadvantages.  
<sup>49</sup> DAS is most sensitive to waves that have particle motion parallel to the orientation of the fiber, so  
<sup>50</sup> it is said that the technology has broadside insensitivity. Multi-component geophones also have this  
<sup>51</sup> issue; with more recording components, however, they are able to resolve more of the wavefield and  
<sup>52</sup> are not affected by this broadside insensitivity as much.

<sup>53</sup> Another disadvantage is that DAS coupling is not trivial in all environments. In a borehole  
<sup>54</sup> environment, DAS can be cemented behind casing or permanently installed on production tubing  
<sup>55</sup> (Mateeva et al., 2013). Surface distributed sensor coupling is a more challenging issue. Lindsey  
<sup>56</sup> et al. (2017) describe how fibers can be utilized in loosely coupled environments. The Stanford  
<sup>57</sup> Fiber Optic Array consists of a 2.5 km long array that lies in a conduit about 1 to 2 meters below  
<sup>58</sup> ground. The DAS fiber geometry is restricted by the conduits, though, and the task of installing the  
<sup>59</sup> fiber is more difficult if there are no existing conduits. Daley et al. (2013) have trenched the cable  
<sup>60</sup> and returned at a later time to shoot the seismic survey. Although this method is effective, waiting  
<sup>61</sup> to shoot a survey at a later time can be inconvenient.

<sup>62</sup> **Previous Work**

<sup>63</sup> Historically, DAS has been used in a borehole environment for flow monitoring, temperature mea-  
<sup>64</sup> surements, and vertical seismic profiles (Clarke and Sandberg, 1983; Krohn et al., 2000; Mestayer  
<sup>65</sup> et al., 2011; Barberan et al., 2012; Cox et al., 2012; Daley et al., 2013; Mateeva et al., 2014).

<sup>66</sup> Mestayer et al. (2011) describe how permanently installed fiber-optic infrastructure in existing  
<sup>67</sup> wells can enable low-cost non-intrusive geophysical monitoring. Geophones generally only acquire  
<sup>68</sup> data along a short subset of the well due to the limited number of receivers at predetermined receiver

spacing in VSP receiver arrays. This makes repeatable time-lapse surveys difficult as placing the geophones in the same location is not trivial. Mestayer et al. (2011) also discuss how borehole DAS is able to improve repeatability and time-lapse sensitivity because it is able to acquire data along the full well with a single shot. Mateeva et al. (2014) also describe a time lapse, 3D DAS VSP application. They conclude that DAS has many major business impacts on fields that require enhanced oil recovery (EOR) including cost efficiency, safety, and synergy with other fiber optic applications.

Barberan et al. (2012) discuss different ways DAS fiber can be coupled in a borehole environment. DAS fiber can be clamped to production tubing and used as a downhole seismic sensor. Barberan et al. (2012) expand on this explaining that acquiring seismic data over the entire well is essential for acquiring additional transit times for velocity inversion and it allows for a wide range of incidence angles in terms of wave directions that arrive at the fiber for inversion.

Daley et al. (2013) describes field tests from both horizontal and borehole distributed sensors. They conclude that the signal-to-noise (SNR) in surface DAS is not sufficient for observing P-waves and that DAS is more useful in borehole environments or longer surface arrays. They don't go into detail, however, regarding why certain waves are not observable in DAS.

As seen in these examples, DAS research has emphasized acquiring data in borehole environments because many wells are already equipped with fiber for production. As a result, acquiring DAS in boreholes is as simple as connecting the existing fiber-optic cable to a new interrogator unit that senses acoustic signal. Although there are some studies on surface DAS acquisitions (Daley et al., 2013; Hornman, 2017), there has not been a thorough study in active source experiments.

Daley et al. (2013) experiment with a vertical vibrator (vertical-force) source. The reflected P-wave is not recorded on the DAS fiber as the experiment only had 1,000 meters of offset, and,

92 therefore, the authors concluded that the SNR in surface DAS is insufficient for observing P-waves  
93 due to the relatively small incidental reflected angle. Other source mechanisms must be investigated  
94 before such a conclusion can be made about the feasibility of using surface DAS fiber. Another  
95 option is utilizing the DAS fiber along with geophones to attempt to minimize the insensitivity of  
96 some waves. This paper explores different imaging experiments using the field geometry from the  
97 PoroTomo survey in Northwest Nevada and numerical modeling to explain how DAS fiber can help  
98 minimize the insensitivity to waves in conjunction with geophones. The objective of these experi-  
99 ments is to analyze if the densely sampled DAS fiber data can help improve the image produced by  
100 the sparsely sampled geophones.

## 101 **PoroTomo Survey**

102 The PoroTomo survey involved four-weeks of data acquisition of geodesy, interferometric syn-  
103 thetic aperture radar (InSAR), hydrology, temperature sensing, passive source seismology, and ac-  
104 tive source seismology data (Feigl, 2017; Cardiff et al., 2018). The variety of data that were col-  
105 lected at the PoroTomo survey lead to the origin of the experiments name: Poroelastic Tomography  
106 by Adjoint Inverse Modeling of Data from Seismology, Geodesy, and Hydrology (or PoroTomo for  
107 short). These data were jointly collected to characterize and monitor changes in the rock mechanical  
108 properties of Brady's Natural Laboratory (BNL), an Enhanced Geothermal System (EGS) reservoir.

109 This paper investigates the active seismic source component of the PoroTomo Experiment. The  
110 PoroTomo survey is one of the most unique seismic acquisitions for surface DAS fiber. The survey  
111 included 238 multi-component geophones, 156 three-component (vertical and orthogonal horizon-  
112 tal) vibroseis source locations that swept from 5 to 80 Hz in 20 seconds, 300 meters of borehole  
113 DAS, and nearly nine kilometers of surface fiber-optic cable. The full survey geometry is shown in

114 Figure 1. As seen in Figure 1, the geophones are sparsely spaced with an average inline spacing of  
115 80 meters. This paper focuses on identifying a methodology to resolve the spatial sampling issue.  
116 The objective of this paper is to identify if the densely sampled DAS data can help improve the  
117 image produced by the sparsely sampled geophones. Both 2D and 3D numerical experiments are  
118 performed to test the feasibility of using the broadside sensitivity of multi-component geophones  
119 and the dense sampling DAS data together to minimize insensitivity to certain waves.

## FIBER SENSITIVITY

120 Understanding how DAS fiber works is essential to working with the data that are currently available  
121 and to design effective future surveys. For a conventional DAS seismic survey, a known pulse of  
122 light is sent into the fiber using an interrogator unit and some of the light is naturally scattered back  
123 due to imperfections within the fiber. The interrogator unit is able to record this scattered light along  
124 the fiber up to 10-kilometers away. This is known as the base condition inside of the fiber. The fiber  
125 undergoes a strain when a seismic wavefield approaches and a scattering of light is produced that is  
126 different from the base condition. The interrogator unit is able to relate this new scattering of light  
127 to local strain along the fiber by recording the time of arrival and the phase-lag of the returning light  
128 signals (Parker et al., 2014).

129 DAS fiber is most sensitive to waves that are able to stretch and squeeze the fiber, so the waves  
130 have to have particle motion parallel to the orientation of the fiber. Every seismic sensor has its own  
131 distinct sensitivity to the various types of waves depending on their emergent angle. The emergent  
132 angle ( $\theta$ ) represents the angle between the incoming wave and the surface of the Earth. Consider a  
133 plane wave reflection in the X-Z plane: an emergent angle of  $0^\circ$  represents a wave arriving parallel  
134 to the surface (or a plane wave traveling in the Z-direction); an emergent angle of  $90^\circ$  represents a

135 wave arriving perpendicular to the surface (or a plane wave traveling in the X-direction).

136 These points can be demonstrated with a simple 2D example. Consider wave propagation in  
137 the X-Z plane in a homogeneous, flat-layered, isotropic or vertical transverse isotropic medium  
138 (Figure 2a-2b). The horizontal DAS fiber is oriented in the x-direction. P-waves have particle  
139 motion parallel to the direction of wave propagation (Aki and Richards, 1980). Normal-incidence  
140 reflections from a horizontal reflector will arrive perpendicular to the surface fiber. Data will not  
141 be seen at short offsets in the case of a reflected P-wave (Figure 2a). The particle motion of P-  
142 waves is parallel to the direction of propagation, so at short offsets, the reflected P-wave will arrive  
143 perpendicular to the fiber. As seen in Figure 3a, P-waves with a  $0^\circ$  emergent angle show zero  
144 amplitude on the fiber and maximum amplitude on the z-component of a geophone, following a  
145  $\cos^2(\theta)$  decay with emergent angle ( $\theta$ ). Moving to further offsets yields emergent angles that are  
146 at a larger angle to the fiber. According to Figure 3a, these waves will show more data than waves  
147 arrive perpendicular to the fiber as they are propagating in the direction of the fiber and will show  
148 less data on the vertical component of the geophone. The further the offset, however, the lower the  
149 amplitude of the wave due to attenuation effects.

150 Shear-waves are potentially more interesting when recording with horizontal fiber. Consider  
151 again 2D wave propagation in the X-Z plane in a homogeneous, flat-layered, isotropic or vertical  
152 transverse isotropy medium (Figure 2b). SV-waves have particle motion in the X-Z plane, as do  
153 P-waves (Aki and Richards, 1980). Normal-incidence reflections from a horizontal reflector will  
154 arrive perpendicular to the surface fiber. P-wave particle motion, as stated previously, will be in the  
155 z direction, and consequently, will not be recorded by the fiber. SV wave particle motion will be  
156 in the x-direction (emergent angle of  $0^\circ$ ), and the DAS response will be maximum (Figure 3b). At  
157 larger offsets, the SV-wave emerging angle begins to approach  $90^\circ$ . A larger emerging angle means  
158 less signal (Figure 3b) is recorded by both the surface DAS and the x-component of the geophone

159 because the SV-wave particle motion is in the vertical perpendicular to the fiber (Figure 2b).

160 We also consider using SH-waves with the same 2D survey geometry (homogeneous, flat-  
161 layered, isotropic). S-H waves have particle motion perpendicular to the direction of wave propa-  
162 gation or, in this case, in the y-direction. The DAS response to SH-waves will be zero since the SH  
163 particle motion is perpendicular to the DAS fiber, in the y-direction. In this 2D case, the SH-wave  
164 will be out of plane regardless of source-receiver offset. In 3D, SH-waves can be seen on the DAS  
165 if they are properly oriented. For example, a source-receiver azimuth perpendicular to the 2D fiber  
166 (in this case, in the y-direction) will produce a maximum amplitude reflection on the DAS since  
167 the particle motion is in the x-direction for all offsets. As the source-receiver azimuth moves inline  
168 with the fiber, the SH-wave particle motion decreases, and is equal to zero when the source-receiver  
169 azimuth is inline with the fiber.

170 In this section, DAS fiber directionality was described analytically and depicted graphically.  
171 The directionality is important to understand when creating a seismic survey geometry to assist  
172 with geophone deficiencies.

## 2D NUMERICAL MODELING EXAMPLES

173 Imaging the geophone data is a difficult task in the PoroTomo Survey due to the irregular spatial  
174 sampling and offset. This paper focuses on identifying a way to resolve the spatial sampling issue.  
175 Fortunately, the PoroTomo survey includes surface DAS cable that has 10-meter gauge-length and  
176 an equivalent of 1-meter receiver spacing along the fiber. Many papers in the literature are interested  
177 in methods to convert DAS measurements (strain or strain rate) to a geophone equivalent (particle  
178 velocity or displacement) with the intent to replace point sensors with distributed sensors, or use  
179 existing geophone processing to clean up DAS data (Daley et al., 2013, 2015; Jreij et al., 2017).

180 The idea of using both data types in simultaneous imaging is explored in this paper to produce more  
181 detailed images using synthetic examples.

182 **2D Synthetic Design**

183 Siler and Faulds (2013) mapped the faults of Brady's Natural Lab shown in Figure 4. It is important  
184 to image these faults in detail as they are driving factors behind the recharge of the geothermal  
185 reservoir (Feigl, 2017; Folsom et al., 2018). A slice is taken from the Brady's Natural Lab fault  
186 model (Siler and Faulds, 2013) in the PoroTomo Survey and used as a reflection velocity models.  
187 This slice is shown in Figure 5. The Siler and Faulds (2013) fault model slice is used as a reflectivity  
188 model as it contains a variety of structural dips.

189 Seismic sources in the PoroTomo experiment are not on a uniform grid. In fact, the source  
190 spacing is as large as 150 meters. Seismic illumination describes how much of the subsurface can  
191 be imaged given a source-receiver geometry and velocity model. Illumination in seismic surveys  
192 is highly influenced by source-receiver spacing. For the purpose of this section, a constant source  
193 spacing of 75 meters (which is about the average source spacing in the PoroTomo survey) is used  
194 to minimize migration artifact effects from poor illumination. For the 2D experiments present in  
195 this paper, both vertical and horizontal force sources are modeled to represent a vertically and a  
196 horizontal vibe, respectively, which were also collected at BNL for the PoroTomo field experiment.

197 Reverse time migration (RTM) is the imaging technique that is used for the experiments in this  
198 paper. 2D elastic forward modeling is used to produce strain (as measured by DAS) and displace-  
199 ment (as measured by geophones) data along the surface of our 2D example excited by a vertical  
200 force source. Receivers at every one meter across the experiment are used for recording. As seen  
201 in Figure 1, the PoroTomo survey did not include a straight fiber that was this long. It did include,

202 however, a maximum offset of 1,500-meters across the entire survey. A 2D line of 1,500 meters was  
203 utilized to gather data with similar offsets as the PoroTomo survey.

204 The code generated for these experiments outputs both strain and displacement at every receiver  
205 location. The average geophone spacing is about 70 meters in the PoroTomo experiment. A geo-  
206 phone spacing of 100 meters is chosen to analyze geophone spacing closer to the extremes of this  
207 experiment. The recorded data are generated from a reflectivity model that is derived from Brady's  
208 fault model using an elastic finite difference modeling (FDM) operator from the Madagascar pack-  
209 age (Fomel et al., 2013). The next step is to back propagate the recorded data from this forward  
210 modeling to recover the receiver wavefield. If this was a field experiment, the field data would be  
211 back propagated. Two different sources are needed to create the receiver wavefield. An acceleration  
212 force is used for back propagation of the geophone data and a stress tensor is used for back propaga-  
213 tion of the DAS data. The proper way to do imaging is to back propagate the two data types (strain  
214 and displacement) simultaneously, but this was not possible with current codes, so the data are back  
215 propagated individually.

216 The last wavefield that needs to be generated is the source wavefield. The source wavefield is a  
217 forward model from the original source location through a smooth velocity model. It is important  
218 that the velocity model is smooth as reflections will cause an improper final image. Now, a source  
219 and two receiver wavefields exist. An imaging condition is required to combine the wavefields.

220 Traditionally, the zero-lag, cross correlation imaging condition (IC) is used to create a migrated  
221 image (Claerbout, 1985). Although this methodology may provide a solution for elastic imaging,  
222 this IC produces four resulting images (PP, PS, SP, SS). This proves to be a more difficult compari-  
223 son between different data types for the purpose of this paper. Rocha et al. (2016) describes the use  
224 of an energy-norm based IC that exploits wavefield directionality to create a single elastic image

225 that represents the measure of reflected energy. There are many other benefits to using the energy-  
226 norm IC, but most important for this work is that one final image allows for an easy comparison of  
227 migrated elastic data.

228 The image produced from the elastic energy norm RTM with sparsely sampled multi-component  
229 geophones using a vertical force is shown in Figure 6a. This image shows reflectors are discontin-  
230 uous and difficult to follow. The image is also covered with migration artifacts due to insufficient  
231 sampling of the wavefield. An example of this is presented around 800 meters on the x-axis of  
232 Figure 6a: the migration artifacts make it difficult for an interpreter to follow the shallow reflector.  
233 The deeper reflector in Figure 6a is impossible to identify.

234 The image produced from the elastic energy norm RTM with DAS fiber along the surface of the  
235 model creating a virtual receiver at every one meter is shown in Figure 6b. The shallow reflector in  
236 this image is sharp and continuous, allowing for easy interpretation. Although migration artifacts  
237 are still present around 800 meters on the x-axis, these are different from those experienced in  
238 Figure 6a. These migration artifacts are now due to fake modes present because the wavefield is  
239 extrapolated using only the x-component data that was recorded with DAS fiber.

240 Now there are two images with two different migration artifacts (i.e. types of noise). Stacking  
241 the images should theoretically reduce the noise and highlight the reflection events. Linearly stack-  
242 ing the events, however, will not currently work as the amplitudes are on different scales. Instead,  
243 the amplitudes of both images are normalized by the maximum and then stacked to produce Fig-  
244 ure 6c. Although Figure 6c still has artifacts in it, the reflectors are enhanced and the image is easier  
245 to interpret than Figure 6a or Figure 6b.

246 Fiber attributes were discussed earlier in this paper. Different source types can generate different  
247 polarizations of reflection events. For this reason, the second 2D experiment uses the same geometry

248 and model as the first experiment, but now an horizontal force is used to generate data. The image  
249 produced from elastic energy norm RTM with sparsely sampled multi-component geophones and  
250 a horizontal force is shown in Figure 7a. This image still shows some discontinuity in reflectors,  
251 but the reflector is much easier to follow. The receiver sampling was not changed, so the image is  
252 still covered with migration artifacts due to insufficient sampling of the wavefield. On the left-hand  
253 side of the geophone image, the end of the dipping fault is not properly imaged. This is due to  
254 insufficient aperture in the migration. The deeper reflector is now easier to identify in Figure 7a.

255 The image produced from elastic energy norm RTM with DAS data and an S-source is shown  
256 in Figure 7b. The DAS image is still very sharp, but now the migration artifacts have diminished.  
257 The deeper reflector is much easier to observe and interpret as well. This image is sharp because the  
258 zero-offset SV-wave reflections are perfectly polarized to show the reflectors on DAS and the DAS  
259 data is really well sampled.

260 There are two images with two different migration artifacts (i.e. types of noise), so the images  
261 are normalized and stacked just as it was done for the previous example. The results are shown in  
262 Figure 7c. Figure 7c shows both reflectors clearer than Figure 6c which suggests that a horizontal  
263 force is more beneficial for near-offset DAS surveys.

## 264 **Value of Information**

265 All of the experiments presented in the paper can be qualitatively analyzed and discussed, but qual-  
266 itative analysis is always different between people due to different biases and perspectives. A method  
267 to quantitatively analyze the experiments is needed to do effective comparisons.

268 The Value of Information (VOI) is a quantitative tool that originates from the field of decision  
269 analysis to quantify how relevant and reliable an information source is (Trainor-Guitton et al., 2013).

270 VOI estimates the possible increase in expected utility by gathering information. It is calculated by  
 271 comparing the prior value ( $V_{prior}$ , the average utility of a decision made with current information)  
 272 to the value with imperfect information ( $V_{imperfect}$ ) by subtracting the two, shown in Equation 1.

$$VOI = V_{imperfect} - V_{prior} \quad (1)$$

273 The goal of this project is to observe if there is any added value to using distributed acoustic  
 274 sensing in surface acquisitions. The value with imperfect information shown in Equation 2 can only  
 275 be calculated with a quantitative measure of how accurate the information source as,

$$V_{imperfect} = \sum_{j=F,NF} Pr(\theta^{int} = \theta_j) \max_a [ \sum_{i=F,NF} Pr(\theta = \theta_i | \theta^{int} = \theta_j) v_a(\theta_i) ] \quad (2)$$

276 This quantitative measure can be represented by the posterior probability,  $Pr(\theta = \theta_i | \theta^{int} = \theta_j)$ ,  
 277 within the value with imperfect information (Equation 2). Specifically for these problems, the  
 278 posterior probability can be how often interpretations of faults align with the actual presence of  
 279 faults. It is important to calculate the posterior reliability so the value of imperfect information can  
 280 be completed. The posterior probability can be calculated using Equation 3,

$$Pr(\theta = \theta_i | \theta^{int} = \theta_j) = \frac{(Pr(\theta = \theta_i)) Pr(\theta^{int} = \theta_j | \theta = \theta_i)}{Pr(\theta^{int} = \theta_i)}; \forall i, j = F, NF \quad (3)$$

281 where  $\theta$  represents a true value of Fault or Not Fault,  $\theta^{int}$  represents an interpreted Fault or Not  
 282 Fault. There are a variety of methodologies to produce information about whether an interpreted  
 283 fault is actually a fault or not. This paper utilizes a machine learning approach to interpret the  
 284 features in the migrated image.

285 **Convolutional Neural Network Analysis**

286 Machine learning is a field within computer science that focuses on the ability of computer systems  
287 to learn patterns within data without being explicitly programmed for these patterns (Samuel, 1959).  
288 Machine learning has had a large boom in the geophysics industry within the last 10 years.

289 There are a variety of machine learning algorithms that can be utilized based on the problem that  
290 needs to be solved. One of the most powerful machine learning algorithms is the neural network.  
291 Neural networks are inspired by the biological neural networks that constitute human brains or at  
292 least how humans perceive they work (Gerven and Bohte, 2018). They consist of many layers in  
293 parallel and every layer consists of a number of nodes. All neural networks consist of at least two  
294 layers: the input layer and output layer. All the extra layers in between the input and output layers  
295 are the hidden layers. The nodes of every layer are like neurons in the brain. Every neuron has its  
296 own activation function that determines whether it should be “fired” or not similar to how a neuron  
297 in the brain behaves. Each layer receives the output from the previous layer based on if the previous  
298 neuron is fired or not.

299 Convolutional Neural Networks (CNN) in particular are at the core of most state-of-the-art com-  
300 puter vision solutions for a wide variety of tasks. One of the most accurate CNN image classifiers  
301 is the Inception-v3 model (Szegedy et al., 2015). The original Inception-v3 model is trained and  
302 tested on the 2012 ImageNet Large Scale Visual Recognition Challenge (Russakovsky et al., 2015).  
303 The training dataset consisted of 10,000,000 labeled images that depicted 1,000 object categories.  
304 The Inception-v3 model was able to perform with 3.5% top-5 error, meaning that the target label  
305 is within the top-5 probability classifications that the algorithm produced. A top-5 error of 3.5%  
306 means the Inception-v3 model is able to perform with high accuracy, making it a top contender for  
307 a geophysics image classification problem.

308        The Inception-v3 model utilizes transfer learning which means it stores knowledge gained from  
309    training on the ImageNet dataset and then applies it to a different but related problem. It is difficult to  
310    train a CNN from scratch because a large dataset is needed with a substantial amount of computers  
311    equipped with GPU's. Instead, the intermediate layers of the Inception-v3 model are used as they  
312    are already trained on detecting edges, shapes, and other high level features. The weights of the  
313    model's last layer are recreated to identify if an image is either a fault or not a fault.

314        The Inception v3 model's ability to identify features can be leveraged within the geophysics  
315    realm. The first step is to create some training data to retrain the model. The objective is to see  
316    if DAS helped identify more faults than a sparse array of multi-component geophones. For the  
317    experiments in this chapter, RTM images are created from 2D reflectivity slices of the Siler and  
318    Faulds (2013) fault model. There are about 500 other slices along both the X and Y axis of the  
319    PoroTomo grid. A number of these slices can be migrated to create training data for identifying  
320    faults.

321        The next step is to take spatial windows of the migrated images and label them based on if there  
322    are faults or not within the image. 100 meter by 100 meter (10 grid cell by 10 grid cell) subsets of  
323    the migrated images were created. There are a large amount of data present and individually picking  
324    whether an image contains a fault or not would be time consuming. As stated earlier, the true fault  
325    model exists to compare with the migrated images. The same subset of the migrated images can  
326    be compared with the reflectivity model. If more than half the pixels are a fault, then the program  
327    labels the training data as a fault (Figure 8a). Otherwise, the program labels the training data as not  
328    a fault (Figure 8b).

329        This is an easy and automatic way to generate training data, but training is an essential step  
330    prior to testing, so it needs to be continually improved. The next step is to QC the training data to

331 make sure that the examples are actually of “faults” and “not faults”. Many iterations are required  
332 until an acceptable cross-validation accuracy is achieved. A total of 2500, 100 meter by 100 meter  
333 windowed RTM images were used to train the CNN to detect faults. A final training validation  
334 accuracy of 94.4% is achieved. This is an acceptable accuracy check and now the neural network is  
335 ready to be tested on data that were not included in the training data.

336 A 100 meter by 100 meter testing data is created the same way the training data is created. The  
337 testing data is kept hidden from the training data. The first RTM image that is used for testing is  
338 the vertical source data from the velocity model shown in Figure 5. The first test is on the sparse,  
339 multi-component geophone image (Figure 6a). The RTM image is decomposed into 3,625 (100  
340 meter x 100 meter) images with labels of “Faults” and “Not Faults”. This same process is used for  
341 the synthetic created from DAS and multi-component geophones.

342 A posterior reliability of information can be calculated with the results from the testing data.  
343 The resulting posterior reliability of information is shown graphically in Figure 9a and Figure 9b  
344 for a vertical force and a horizontal force, respectively.

345 The results from Figure 9a for the vertical source show that adding DAS into the sparse array  
346 of geophones with Figure 5 as the velocity model improves the classification of faults by 20%.  
347 However, there is an increase in false negatives by about 30%. This means either the normalized,  
348 stacked image has many artifacts or the classifier needs to be better trained on what is not a fault.  
349 The number of false positives decreases by 20% which is a substantial amount. Lastly, the number  
350 of true negatives decreases by almost 30%. This confirms that the classifier needs to be better trained  
351 on what is not a fault.

352 The results from Figure 9b for the horizontal source show that adding DAS into the sparse array  
353 of geophones with Figure 5 as the velocity model decreases the classification of faults by about 1%.

354 However, the classification of true negatives increases by about 5% and false negatives decreases by  
355 about 5% meaning the DAS data did add some value to the CNN classification.

356 **2D Summary**

357 This section discussed in great detail how 2D DAS data can be modeled. It also showed how a  
358 long offset, 2D surface DAS line can produce a sharp resulting image. A quantitative analysis using  
359 a machine learning methodology showed that DAS does add value to sparse geophone arrays. A  
360 quantitative analysis also shows that using a horizontal force with DAS allows for sharper images.  
361 These hypotheses must now be confirmed with a 3D acquisition.

### 3D NUMERICAL MODELING EXAMPLES

362 The objective of this paper is to observe if there is any added value of using surface DAS with  
363 sparsely sampled, multi-component geophones. In the previous section, we observed that in a long  
364 2D line, there is added value using DAS to help with the spatial sampling. In 3D, however, there  
365 are many more complications than in 2D. This section explores additional examples of using DAS  
366 in combination with multi-component geophones, but now with the PoroTomo 3D survey geometry.  
367 These examples utilize numerical modeling to understand more about what is recorded.

368 A velocity model from sweep interferometry shown in Figure 10 was used to create data (Matzel  
369 et al., 2017a). As in the previous section, a modified version of the conventional elastic FDM code  
370 (ewefdm) present in Madagascar (Fomel et al., 2013) is utilized, but now for the 3D case. This  
371 allows us to recover both displacement and strain data along receivers in the grid. A variable density  
372 is now used to create reflectivity instead of using purely velocity changes to create reflectivity in the  
373 2D case.

374 **3D Modeling of Non-Uniform DAS Acquisition**

375 The wavefield along the fiber is now recorded for the six components of strain (XX, XY, XZ, YY,  
 376 YZ, and ZZ). Field DAS data with single fiber, however, does not recover all six components. In-  
 377 stead, it only recovers contributions of the wavefield in the direction that it is oriented. We can  
 378 project the six components from the synthetic data on to the vector direction of the field fiber loca-  
 379 tions to recover the strain in the direction that the fiber is oriented by using Equation 4,

$$\begin{bmatrix} \varepsilon_{ZZ} \\ \varepsilon_{XX} \\ \varepsilon_{YY} \\ \varepsilon_{XY} \\ \varepsilon_{YZ} \\ \varepsilon_{ZX} \end{bmatrix} = \begin{bmatrix} V_Z^2 & V_X^2 & V_Y^2 & 2V_XV_Y & 2V_YV_Z & 2V_ZV_X \end{bmatrix} = \begin{bmatrix} \varepsilon' \end{bmatrix} \quad (4)$$

380 where  $\varepsilon_{ij}$  is the strain in the direction  $ij$ ,  $V_i$  is the vector projection in the  $i$  direction, and  $\varepsilon'$  is  
 381 the strain in the direction of the fiber.

382 A matrix of fiber vector directions must be created prior to using Equation 4. The fiber endpoints  
 383 were recorded in the field using a handheld GPS device after the fiber was trenched. The virtual  
 384 receiver locations along the fiber were then interpolated at 1-meter spacing between these endpoints.  
 385 Although this gives a good estimate of the x and y coordinates of the fiber, this does not give any  
 386 information on how deep the fiber was trenched. For this reason, we assume that the fiber was  
 387 all trenched in the same horizontal plane and there are no dips along the fiber. This simplifies  
 388 Equation 4 to only have contributions from X and Y.

389 Applying Equation 4 recovers only one value of strain along the fiber. In reality, there are

390 contributions from both X and Y, so the strain matrix should have values at XX, YY, and XY. We  
 391 can use the adjoint operation to recover a vector projection of the strain value from Equation 4. The  
 392 adjoint operation shown in Equation 5 returns back to the original PoroTomo coordinate system.

$$\begin{bmatrix} \varepsilon' \end{bmatrix} = \begin{bmatrix} V_Z^2 \\ V_X^2 \\ V_Y^2 \\ 2V_X V_Y \\ 2V_Y V_Z \\ 2V_Z V_X \end{bmatrix} = \begin{bmatrix} \varepsilon_{ZZ} \\ \varepsilon_{XX} \\ \varepsilon_{YY} \\ \varepsilon_{XY} \\ \varepsilon_{YZ} \\ \varepsilon_{ZX} \end{bmatrix} \quad (5)$$

393 The last attribute of fiber that needs to be modeled is the gauge-length. As discussed earlier  
 394 in this paper, the gauge-length of fiber is related to the wavelength recorded along the fiber and it  
 395 acts as a moving average. The gauge-length in the PoroTomo survey was set at 10-meters, so the  
 396 modeled data,  $d$ , is a matrix multiplication of  $\frac{1}{10}$  for the gauge length, the spatial sampling 1-meter,  
 397 and the raw point data,  $b$ , recorded by the finite difference code (shown in Equation 6, after Lim  
 398 Chen Ning and Sava, 2018).

$$\begin{bmatrix} d_5 \\ d_6 \\ d_7 \\ \vdots \\ d_{n-5} \end{bmatrix} = \frac{1}{10} \begin{bmatrix} 1 & 1 & 1 & 1 & 1 & 1 & 1 & 1 & 1 & 1 & 0 & 0 & 0 & 0 \\ 0 & 1 & 1 & 1 & 1 & 1 & 1 & 1 & 1 & 1 & 1 & 0 & 0 & 0 \\ 0 & 0 & 1 & 1 & 1 & 1 & 1 & 1 & 1 & 1 & 1 & 0 & 0 & 0 \\ 0 & 0 & 0 & \ddots & 0 \\ 0 & 0 & 0 & 0 & 1 & 1 & 1 & 1 & 1 & 1 & 1 & 1 & 1 & 1 \end{bmatrix} \begin{bmatrix} b_5 \\ b_6 \\ b_7 \\ \vdots \\ b_{n-5} \end{bmatrix} \quad (6)$$

399    **Numerical Modeling**

400    It is important to image the faults in detail at Brady's Natural Lab as they are the driving factors  
401    behind the recharge of the geothermal reservoir. Although Siler and Faulds (2013) would be a good  
402    candidate for data modeling, a simpler model is needed to first test the hypothesis of imaging using  
403    the two data types simultaneously. A four layer model with a variety of structures is used as the  
404    density model for the first example (Figure 11). There is a contrast of about 300 g/cc between each  
405    layer to ensure strong reflections.

406       The synthetic images are produced using the same methodology presented in the 2D section.  
407       The results from migrating the DAS data are shown in Figure 12. The results from migrating the  
408       geophone data are shown in Figure 13. A visual reflectivity model shown on the left of both figures  
409       was produced by applying the Laplacian operator on Figure 11 and setting all values to one.

410       At first glance, it seems as if the DAS image does not have any reflectors. It can be compared  
411       to the true reflectivity model shown on the right of Figure 12 to identify the signal in the image. It  
412       is clear that the data recorded by the DAS fiber is too low in frequency to resolve the beds within  
413       the image. This is due to both the velocity field that the experiment used to mimic the PoroTomo  
414       subsurface and the FDM accuracy condition presented in Equation 7.

$$\frac{v_{min}}{f_{max}} > N * \sqrt{dx^2 + dy^2 + dz^2} \quad (7)$$

415       The minimum velocity of approximately 950 m/s from the input velocity field forces the maxi-  
416       mum frequency of the wavelet to be 16 Hz and the peak frequency of the wavelet to be 12 Hz. This  
417       equates to a 12 Hz wavelet and the velocity model corresponds to a wavelength of about 108 meters.

418       The DAS image (Figure 12) is also contaminated by fake modes and migration artifacts (Rocha

419 et al., 2016). Fake modes are expected since the displacement field is incomplete when wavefield  
420 extrapolation was performed as the fiber is only recording one component of strain in the direction  
421 that it is oriented. An inexperienced interpreter would eagerly interpret the fake modes as an area  
422 of interest for further exploration methods.

423 At first glance, the geophone data also appear to have no clear reflection events. The image can  
424 again be compared to the true reflectivity model overlain on the left of Figure 13 to identify the  
425 signal in the image. The geophone image is also limited by the source wavelet that was injected  
426 into the model. Differentiation between the thin beds is not possible using the source wavelet in this  
427 experiment.

428 The geophone image, similar to the DAS image, is also contaminated by migration artifacts.  
429 These migration artifacts, however, are due to the insufficient sampling that creates migration ar-  
430 tifacts on the edge of reflectors. The wavefield is not sampled completely because the geophones  
431 adopted from the PoroTomo survey are placed sparsely around the model (the average geophone  
432 spacing is about 80 meters).

433 **Quantitative Image Comparison**

434 In 2D, a machine learning methodology was used to create a quantitative image comparison. Al-  
435 though 3D CNN's exist, they are not as polished and readily available as are 2D CNN's. Instead, the  
436 data are quantitatively analyzed using energy norm image filtering. Energy norm filtering focuses  
437 on highlighting areas with reflected energy is maximum, so filtering the image based on an applied  
438 limit will highlight where reflections may be coming from as opposed to migration artifacts. The  
439 geophone and DAS images are combined by first normalizing the data types based on their maxi-  
440 mum amplitude. They are then stacked together to test this hypothesis. This image would ideally

Table 1: Confusion matrix for top 90% energy reflected.

Top 90% energy reflected		
	$\theta_R^{int}$	$\theta_{NR}^{int}$
$\theta_R$	184800	1206000
$\theta_{NR}$	346700	1824000

441 highlight continuous reflectors with the densely sampled DAS data and reduce migration artifacts  
 442 by extrapolating the full displacement wavefield with the multi-component geophones.

443 Every model cell that is above an applied limit is assigned a value of 1 and every model box that  
 444 is below the limit is assigned a value of 0. A cell-by-cell comparison between the filtered, multi-  
 445 component geophone image and the original reflectivity model is performed to identify how much  
 446 additional accuracy is gained by adding the DAS data. The results of this cell-by-cell comparison  
 447 are presented in confusion matrix form (Table 1), where  $R$  represents reflections and  $NR$  represents  
 448 not reflections.

449 The confusion matrices assist in calculating the posterior value using Equation 3. The posterior  
 450 value explains the probability that an event which the data type predicted is the event present. The  
 451 posterior can then be used to calculate the utility or value of information added when using DAS  
 452 and geophone versus only geophone with Equation 1. The results for the medium filter, posterior  
 453 values in the four layer model presented in this paper are displayed in Figure 14.

454 In this experiment, adding distributed sensors increases the probability of finding if a cell is not  
 455 a reflector and decreases the probability of false negatives. Adding distributed sensors, however,  
 456 increases the probability of identifying false positives and decreases the probability of finding true  
 457 reflectors. This experiment, however, is inconclusive in identifying if DAS has added value with  
 458 sparsely sampled geophone data. A better DAS geometry must be tested to make further conclusions

459 on the effectiveness of surface DAS fiber.

460 The geometry shown in Figure 15 is utilized to further test the effectiveness of surface DAS  
461 fiber. This new acquisition utilizes 25% less fiber and 60% fewer sources than the PoroTomo survey  
462 geometry. Quantitative analysis using the energy norm filtering methodology is utilized again to  
463 identify how well the survey imaged. The results are presented in Figure 16

464 Figure 16 shows a significant increase in true positives and decrease in false negatives. Al-  
465 though there was an increase in false positives and a decrease in true negatives, the increase in true  
466 positives proves that this new acquisition is better suited to image the subsurface with surface DAS  
467 fibers. Energy norm imaging again allowed for an automatic method to interpret images output  
468 from the migration images. Filtering images based on amplitudes is a crude approximation of how  
469 an interpreter would “interpret” an image.

## 470 **3D Summary**

471 This section discussed differences in modeling DAS data in 3D versus 2D. The experiments in this  
472 section helped clarify what kinds of data that a single surface DAS fiber can record. The experiments  
473 discovered that the DAS configuration in the PoroTomo survey combined with the low frequency  
474 nature of the modeling did not add value to the multi-component geophone imaging effort. Addi-  
475 tionally, the percentages of missing strain components in 3D is larger than the 2D case, contributing  
476 to the poor image quality. A better geometry and multi-component DAS were required to make  
477 further conclusions on the effectiveness of DAS fiber in surface acquisition. Another experiment  
478 was preformed with DAS fibers arranged in 2D lines. This acquisition geometry led to an increased  
479 percentage of reflectors identified. It is concluded that the 2D surface DAS fiber lines are a better  
480 suited geometry to image the subsurface.

## CONCLUSIONS

481 In this paper, we discussed some of the fiber attributes that are essential to understand before looking  
482 at surface DAS data. The most important attribute is the types of waves that fiber is directionally  
483 sensitive. It is concluded that surface DAS in a flat-layered Earth model is sensitive to long offset  
484 P-waves, short offset SV-waves, and SH-waves produced by a source that is perpendicular to the  
485 fiber orientation.

486 It was discovered that the geophone data in the PoroTomo survey was too sparsely sampled, and  
487 the hypothesis that densely sampled DAS data can fill in the gaps of the geophones was introduced.  
488 This hypothesis was tested in 2D using elastic numerical modeling and RTM. It is then shown how  
489 data are modeled for DAS receivers in 2D. The energy norm imaging condition was chosen as it  
490 allowed for an easier method to compare two images than the conventional imaging condition. The  
491 experiments showed that an inline horizontal force allows for the best results qualitatively due to the  
492 resulting SV reflections. Lastly, this section explains the need for statistical and quantitative analysis  
493 in the geophysics realm. A description of how to perform quantitative analysis using machine  
494 learning methodology is presented. Both methods concluded that DAS added imaging value to  
495 sparsely sampled multi-component geophones.

496 The 2D scenario did not test the full DAS fiber directionality. We discuss 3D numerical mod-  
497 eling and RTM used to combine DAS and multi-component geophone data. The challenges of  
498 modeling DAS in 3D are also discussed including recording the proper component of strain along  
499 the fiber. The resulting migrated images did not clarify if DAS added any qualitative value to multi-  
500 component geophone images as the migrated images were too low of a frequency to analyze due  
501 to the limitation of the velocity model. A quantitative analysis of the combined image is utilized.  
502 This chapter concluded that adding DAS data only helped to reduce the number of false positives

503 by a very small fraction. This experiment is inconclusive in regards to identifying if DAS can add  
504 value to sparsely sampled geophone data, so another experiment was performed with 2D surface  
505 DAS fiber lines. The new proposed experiment with long-offset, 2D surface fiber lines concluded  
506 that using the new geometry was better suited for surface DAS acquisitions. The next proposed step  
507 is to test this hypothesis with field data.

## REFERENCES

- 508 Aki, K., and P. G. Richards, 1980, Quantative seismology: Theory and methods: New York, **801**.
- 509 Barberan, C., C. Allanic, D. Avila, J. Hy-Billiot, A. Hartog, B. Frignet, and G. Lees, 2012, Multi-
- 510 offset seismic acquisition using optical fiber behind tubing: Presented at the 74th EAGE Confer-
- 511 ence and Exhibition incorporating EUROPEC 2012.
- 512 Cardiff, M., D. D. Lim, J. R. Patterson, J. Akerley, P. Spielman, J. Lopeman, P. Walsh, A. Singh, W.
- 513 Foxall, H. F. Wang, et al., 2018, Geothermal production and reduced seismicity: Correlation and
- 514 proposed mechanism: Earth and Planetary Science Letters, **482**, 470–477.
- 515 Claerbout, J. F., 1985, Imaging the earth's interior: Blackwell scientific publications Oxford, **1**.
- 516 Clarke, R., and C. L. Sandberg, 1983, Fiber optic temperature sensing. (US Patent 4,417,782).
- 517 Cox, B., P. Wills, D. Kiyashchenko, J. Mestayer, J. Lopez, S. Bourne, R. Lupton, G. Solano, N.
- 518 Henderson, D. Hill, et al., 2012, Distributed acoustic sensing for geophysical measurement, mon-
- 519 itoring and verification: **37**, 7–13.
- 520 Daley, T., D. Miller, K. Dodds, P. Cook, and B. Freifeld, 2015, Field testing of modular borehole
- 521 monitoring with simultaneous distributed acoustic sensing and geophone vertical seismic profiles
- 522 at citronelle, alabama: Geophysical Prospecting.
- 523 Daley, T. M., B. M. Freifeld, J. Ajo-Franklin, S. Dou, R. Pevzner, V. Shulakova, S. Kashikar, D. E.
- 524 Miller, J. Goetz, J. Henninges, et al., 2013, Field testing of fiber-optic distributed acoustic sensing
- 525 (das) for subsurface seismic monitoring: The Leading Edge, **32**, 699–706.
- 526 Feigl, K. L., 2017, Overview and preliminary results from the porotomo project at brady hot springs,
- 527 nevada: Poroelastic tomography by adjoint inverse modeling of data from seismology, geodesy,
- 528 and hydrology: Presented at the Stanford Geothermal Workshop.
- 529 Folsom, M., J. Lopeman, D. Perkin, and M. Sophy, 2018, Imaging shallow outflow alteration to
- 530 locate productive faults in ormats bradys and desert peak fields using csamt.

- 531 Fomel, S., P. Sava, I. Vlad, Y. Liu, and V. Bashkardin, 2013, Madagascar: Open-source software  
532 project for multidimensional data analysis and reproducible computational experiments: Journal  
533 of Open Research Software, **1**.
- 534 Gerven, M. V., and S. Bohte, 2018, Artificial Neural Networks as Models of Neural Information  
535 Processing.
- 536 Hornman, J., 2017, Field trial of seismic recording using distributed acoustic sensing with broadside  
537 sensitive fibre-optic cables: Geophysical Prospecting, **65**, 35–46.
- 538 Hornman, K., B. Kuvshinov, P. Zwartjes, and A. Franzen, 2013, Field trial of a broadside-sensitive  
539 distributed acoustic sensing cable for surface seismic: Presented at the 75th EAGE Conference  
540 & Exhibition incorporating SPE EUROPEC 2013.
- 541 Jreij, S., W. Trainor-Guitton, D. Miller, et al., 2017, Field data comparison of 3d horizontal dis-  
542 tributed acoustic sensing and geophones: SEG Technical Program Expanded Abstracts.
- 543 Krohn, D. A., T. MacDougall, and A. Mendez, 2000, Fiber optic sensors: fundamentals and appli-  
544 cations: Isa.
- 545 Lindsey, N. J., E. R. Martin, D. S. Dreger, B. Freifeld, S. Cole, S. R. James, B. L. Biondi, and J. B.  
546 Ajo-Franklin, 2017, Fiber-optic network observations of earthquake wavefields: Geophysical  
547 Research Letters.
- 548 Mateeva, A., J. Lopez, J. Mestayer, P. Wills, B. Cox, D. Kiyashchenko, Z. Yang, W. Berlang, R.  
549 Detomo, and S. Grandi, 2013, Distributed acoustic sensing for reservoir monitoring with vsp:  
550 The Leading Edge, **32**, 1278–1283.
- 551 Mateeva, A., J. Lopez, H. Potters, J. Mestayer, B. Cox, D. Kiyashchenko, P. Wills, S. Grandi, K.  
552 Hornman, B. Kuvshinov, et al., 2014, Distributed acoustic sensing for reservoir monitoring with  
553 vertical seismic profiling: Geophysical Prospecting, **62**, 679–692.
- 554 Matzel, E., X. Zeng, C. Thurber, Y. Luo, C. Morency, et al., 2017a, Seismic interferometry using

555 the dense array at the brady geothermal field.

556 Matzel, E. M., X. Zeng, C. Thurber, and C. Morency, 2017b, Using Virtual Earthquakes to Charac-

557 terize the Material Properties of the Brady Hot Springs , Nevada: Geothermal Resources Council.

558 Mestayer, J., B. Cox, P. Wills, D. Kiyashchenko, J. Lopez, M. Costello, S. Bourne, G. Ugueto,

559 R. Lupton, G. Solano, et al., 2011, Field trials of distributed acoustic sensing for geophysical

560 monitoring, *in* SEG Technical Program Expanded Abstracts 2011: Society of Exploration Geo-

561 physicists, 4253–4257.

562 Parker, T., S. Shatalin, and M. Farhadiroushan, 2014, Distributed Acoustic Sensing - A new tool for

563 seismic applications: First Break, **32**, 61–69.

564 Rocha, D., N. Tanushev, and P. Sava, 2016, Isotropic elastic wavefield imaging using the energy

565 norm: Geophysics, **81**, S207–S219.

566 Russakovsky, O., J. Deng, H. Su, J. Krause, S. Satheesh, S. Ma, Z. Huang, A. Karpathy, A. Khosla,

567 M. Bernstein, A. C. Berg, and L. Fei-Fei, 2015, ImageNet Large Scale Visual Recognition Chal-

568 lenge: International Journal of Computer Vision (IJCV), **115**, 211–252.

569 Samuel, A. L., 1959, Some studies in machine learning using the game of checkers: IBM Journal

570 of research and development, **3**, 210–229.

571 Siler, D. L., and J. E. Faulds, 2013, Three-dimensional geothermal fairway mapping: Examples

572 from the western great basin, usa,: GRC Transactions, **7**, 327–332.

573 Szegedy, C., V. Vanhoucke, S. Ioffe, J. Shlens, and Z. Wojna, 2015, Rethinking the Inception Ar-

574 chitecture for Computer Vision.

575 Trainor-Guitton, W. J., A. Ramirez, X. Yang, K. Mansoor, Y. Sun, and S. Carroll, 2013, Value

576 of information methodology for assessing the ability of electrical resistivity to detect co2/brine

577 leakage into a shallow aquifer: International Journal of Greenhouse Gas Control, **18**, 101–113.

## LIST OF FIGURES

578        1      PoroTomo survey geometry. Green dots represent source locations, red dots represent geo-

579      phone locations, and the blue line represents the surface DAS layout.

580        2      Consider a source that generates both P and S waves; this is a 2D Homogeneous, flat-

581      layered, isotropic ray path example. The blue lines represent ray paths of the labeled waves, the

582      blue arrow represents the propagation direction of the wave, the green line represents a horizontal

583      reflector in the subsurface, and the yellow star represents the source. (a) Demonstration of P-P wave

584      effect on the fiber using ray paths. Particle motion is inline with propagation direction (blue arrow).

585      The fiber will only record data at large offsets. (b) Demonstration of SV-SV wave effect on the fiber

586      using ray paths. Particle motion is perpendicular with the propagation direction (green arrows). The

587      fiber will only record data at short offsets.

588        3      Amplitude versus emerging angle for both geophone (blue) and horizontal DAS (red). An

589      emerging angle of  $0^\circ$  indicates a wave that is propagating perpendicular to the surface and an emerg-

590      ing angle of  $90^\circ$  degrees indicated a wave is propagating parallel to the surface. (a) Sensitivity with

591      respect to a P-wave at different emerging angles of horizontal DAS (red) and geophone z-component

592      (blue). (b) Sensitivity with respect to an SV-wave at different emerging angles of horizontal DAS

593      (red) and geophone x-component (blue).

594        4      Siler and Faulds (2013) fault density mapping within the PoroTomo Survey box. This

595      model was used as a reflectivity model for the experiments within this section.

596        5      Reflectivity model from Siler and Faulds (2013) extracted at the location of Well 56-A1

597      used for simulating data. Blue dots represent source locations and the red dots represent geophone

598      locations. DAS fiber was placed between the geophone locations.

599        6      (a) Resulting image from migrating geophone synthetic data. (b) Resulting image from

600      migrating DAS synthetic data. (c) Combined image from migrating DAS and geophone synthetic

601 data.

602 7 (a) Resulting image from migrating geophone synthetic data. (b) Resulting image from  
603 migrating DAS synthetic data. (c) Combined image from migrating DAS and geophone synthetic  
604 data.

605 8 (a) Examples of the automatically generated faults images used to train the CNN. (b) Ex-  
606 amples of the automatically generated images that were not faults used to train the CNN.

607 9 Posterior reliability of information from CNN's calculated using Equation 3 using (a) a  
608 vertical force and (b) a horizontal force. The objective is to maximize the percentages of true posi-  
609 tives and negatives (green arrows) while minimizing the percentages of false positives and negatives  
610 (red arrows). This is obtained by having better instruments as well as better classification.

611 10 Body wave (P-wave) velocity (m/s) model from sweep interferometry in 3D perspective  
612 (Matzel et al., 2017b).

613 11 Four layer model with a variety of structures used for data modeling. This model is used  
614 as a density model for elastic modeling.

615 12 Results of migrating the reflectivity model (Figure 11) using the PoroTomo DAS acquisi-  
616 tion shown on the right. The true reflectivity model is overlain and shown on the left. The slices on  
617 each side are taken at the yellow cross shown on the map view of the acquisition.

618 13 Results of migrating the reflectivity model (Figure 11) using the PoroTomo geophone ac-  
619 quisition shown on the right. The true reflectivity model is overlain and shown on the left. The  
620 slices on each side are taken at the yellow cross shown on the map view of the acquisition.

621 14 Posterior reliability of information from energy norm filtering calculated using Equation 3  
622 using a horizontal force. The objective is to maximize the percentages of true positives and nega-  
623 tives (green arrows) while minimizing the percentages of false positives and negatives (red arrows).

624 15 New survey geometry proposed to test the effectiveness of surface DAS fiber. Green dots

625 represent source locations, red dots represent geophone locations, and the blue lines represent the  
626 surface DAS acquisition.

627 16 Posterior reliability of information using a horizontal force and the Figure 15 acquisition  
628 geometry.

629

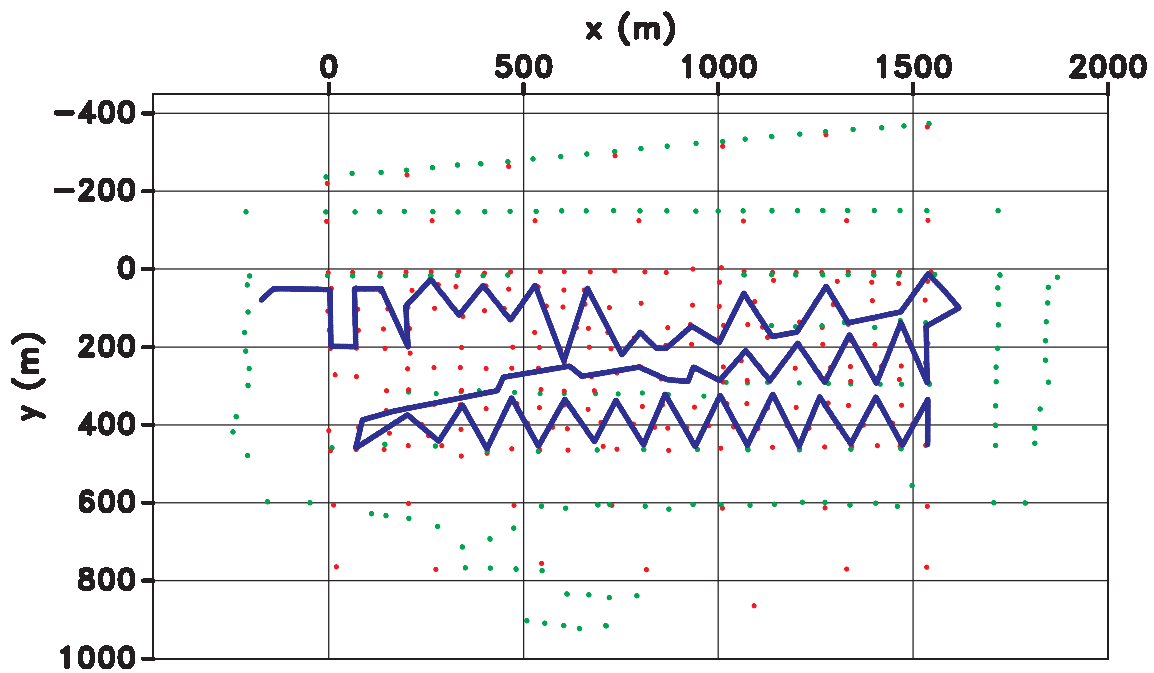
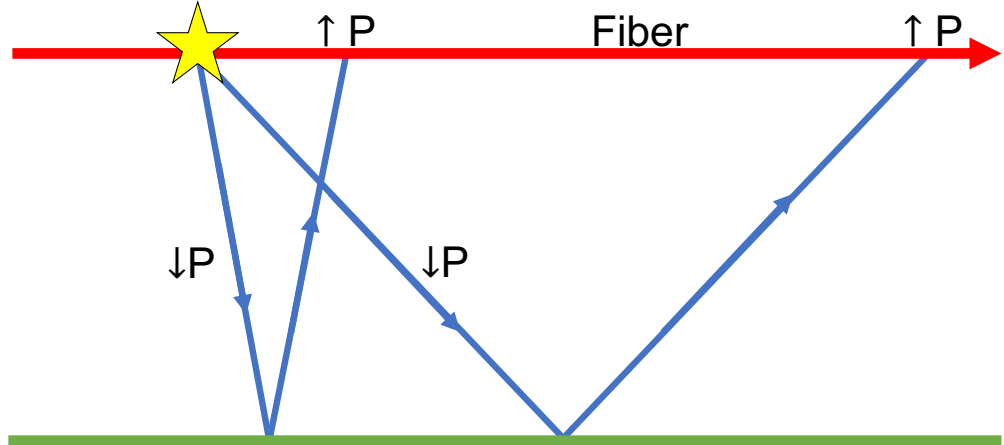
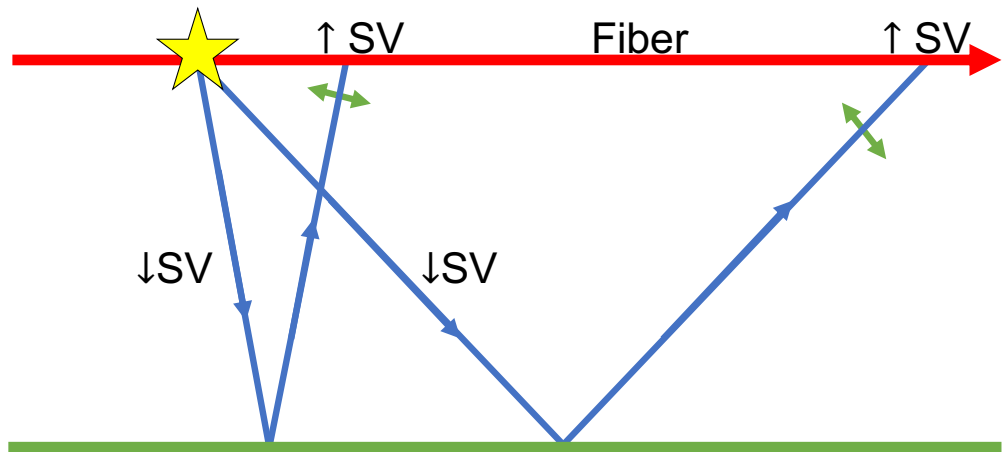


Figure 1: PoroTomo survey geometry. Green dots represent source locations, red dots represent geophone locations, and the blue line represents the surface DAS layout.



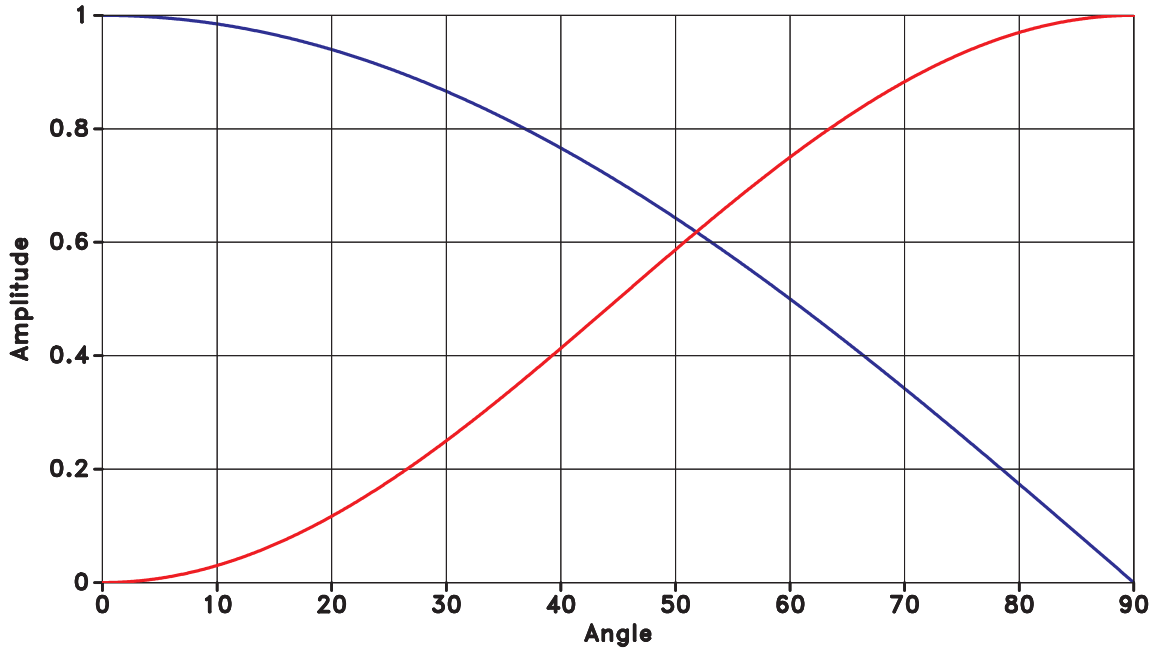
(a)



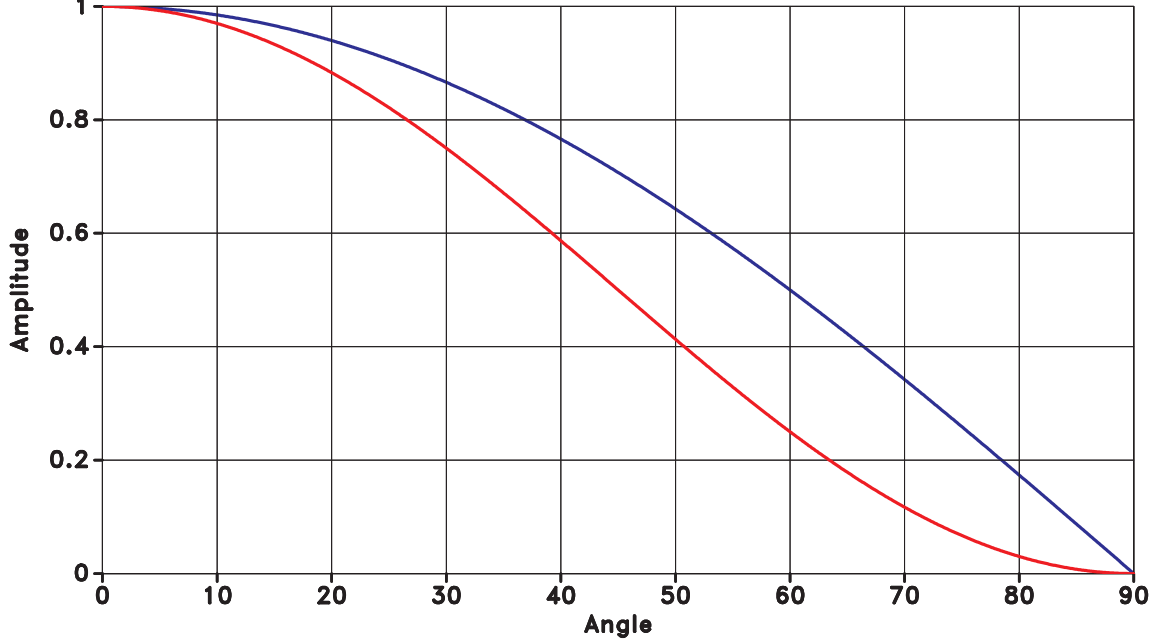
(b)

Figure 2: Consider a source that generates both P and S waves; this is a 2D Homogeneous, flat-layered, isotropic ray path example. The blue lines represent ray paths of the labeled waves, the blue arrow represents the propagation direction of the wave, the green line represents a horizontal reflector in the subsurface, and the yellow star represents the source. (a) Demonstration of P-P wave effect on the fiber using ray paths. Particle motion is inline with propagation direction (blue arrow). The fiber will only record data at large offsets. (b) Demonstration of SV-SV wave effect on the fiber using ray paths. Particle motion is perpendicular with the propagation direction (green arrows). The fiber will only record data at short offsets.

-



(a)



(b)

Figure 3: Amplitude versus emerging angle for both geophone (blue) and horizontal DAS (red). An emerging angle of  $0^\circ$  indicates a wave that is propagating perpendicular to the surface and an emerging angle of  $90^\circ$  degrees indicated a wave is propagating parallel to the surface. (a) Sensitivity with respect to a P-wave at different emerging angles of horizontal DAS (red) and geophone z-component (blue). (b) Sensitivity with respect to an SV-wave at different emerging angles of horizontal DAS (red) and geophone x-component (blue).

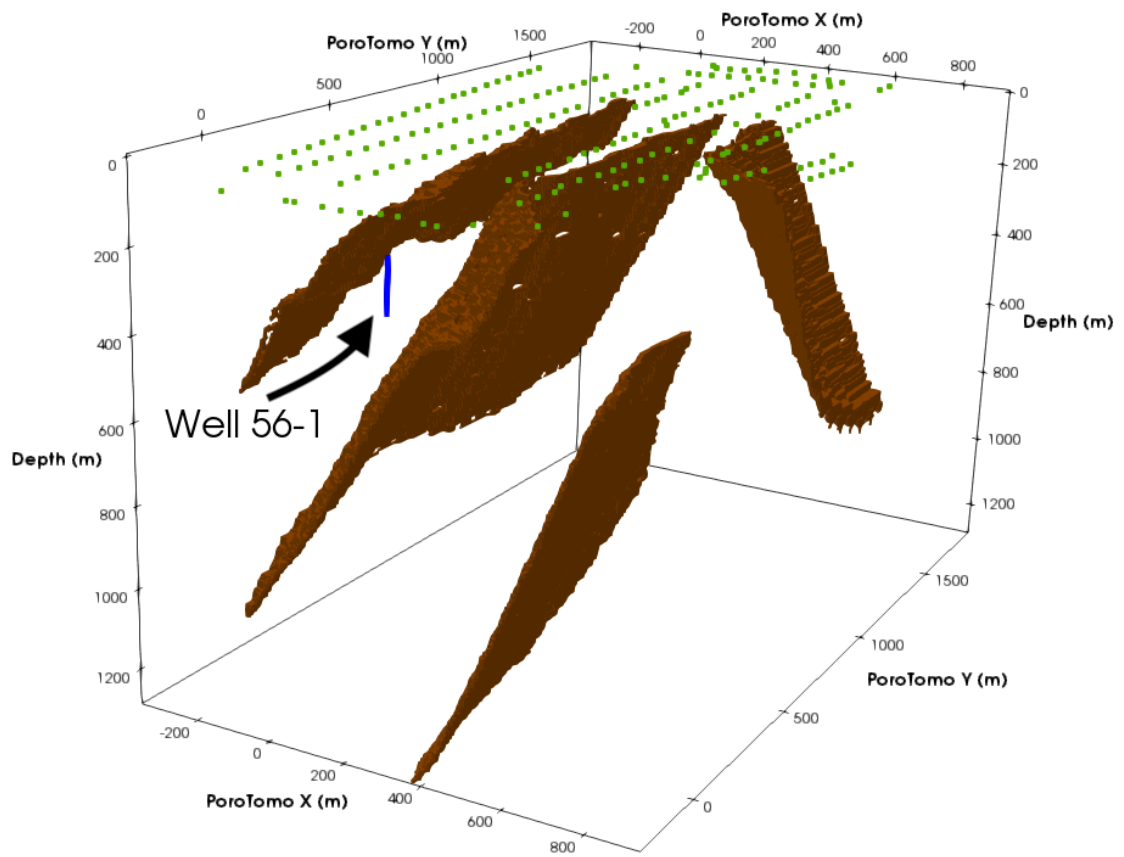


Figure 4: Siler and Faulds (2013) fault density mapping within the PoroTomo Survey box. This model was used as a reflectivity model for the experiments within this section.

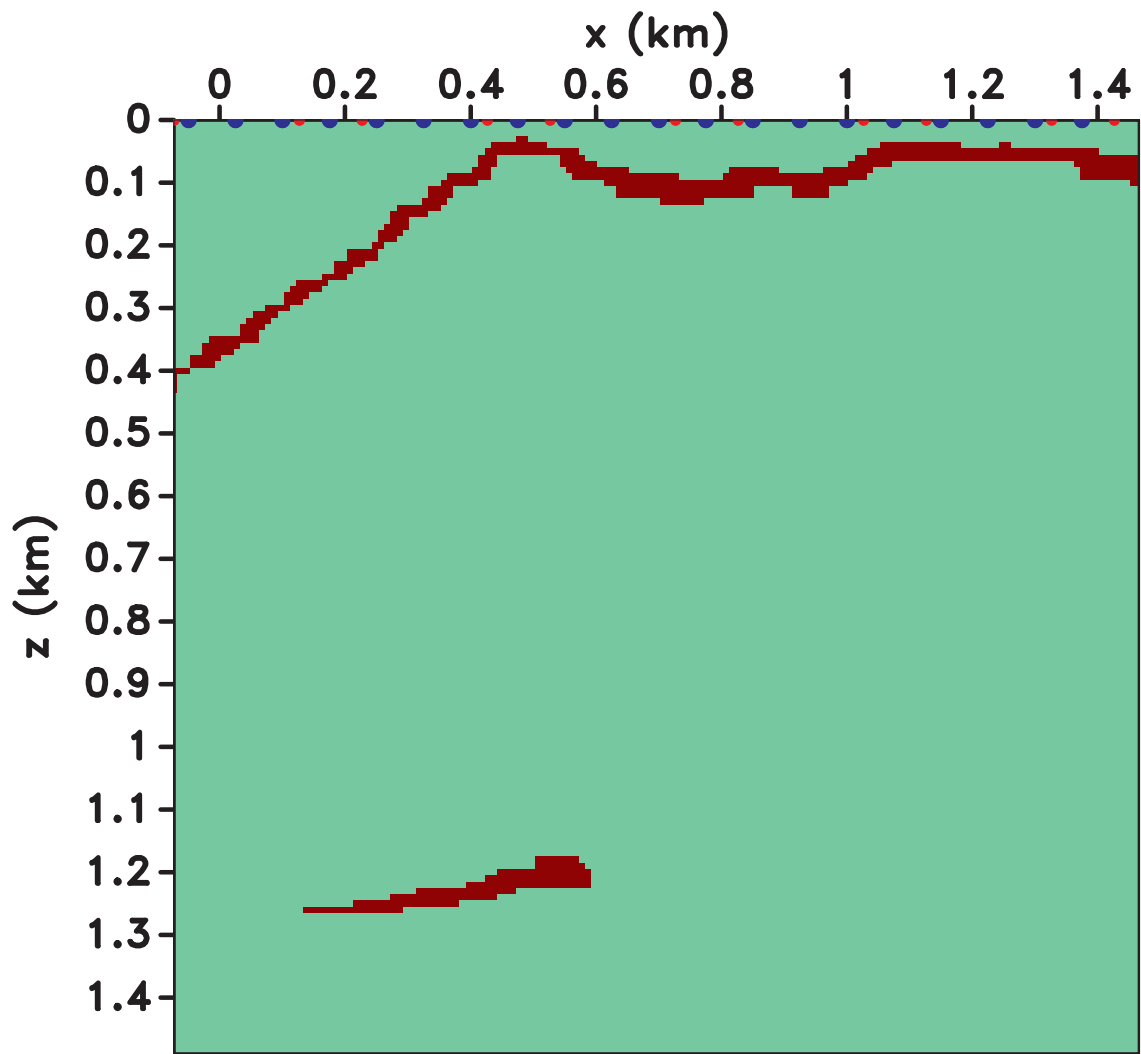


Figure 5: Reflectivity model from Siler and Faulds (2013) extracted at the location of Well 56-A1 used for simulating data. Blue dots represent source locations and the red dots represent geophone locations. DAS fiber was placed between the geophone locations.

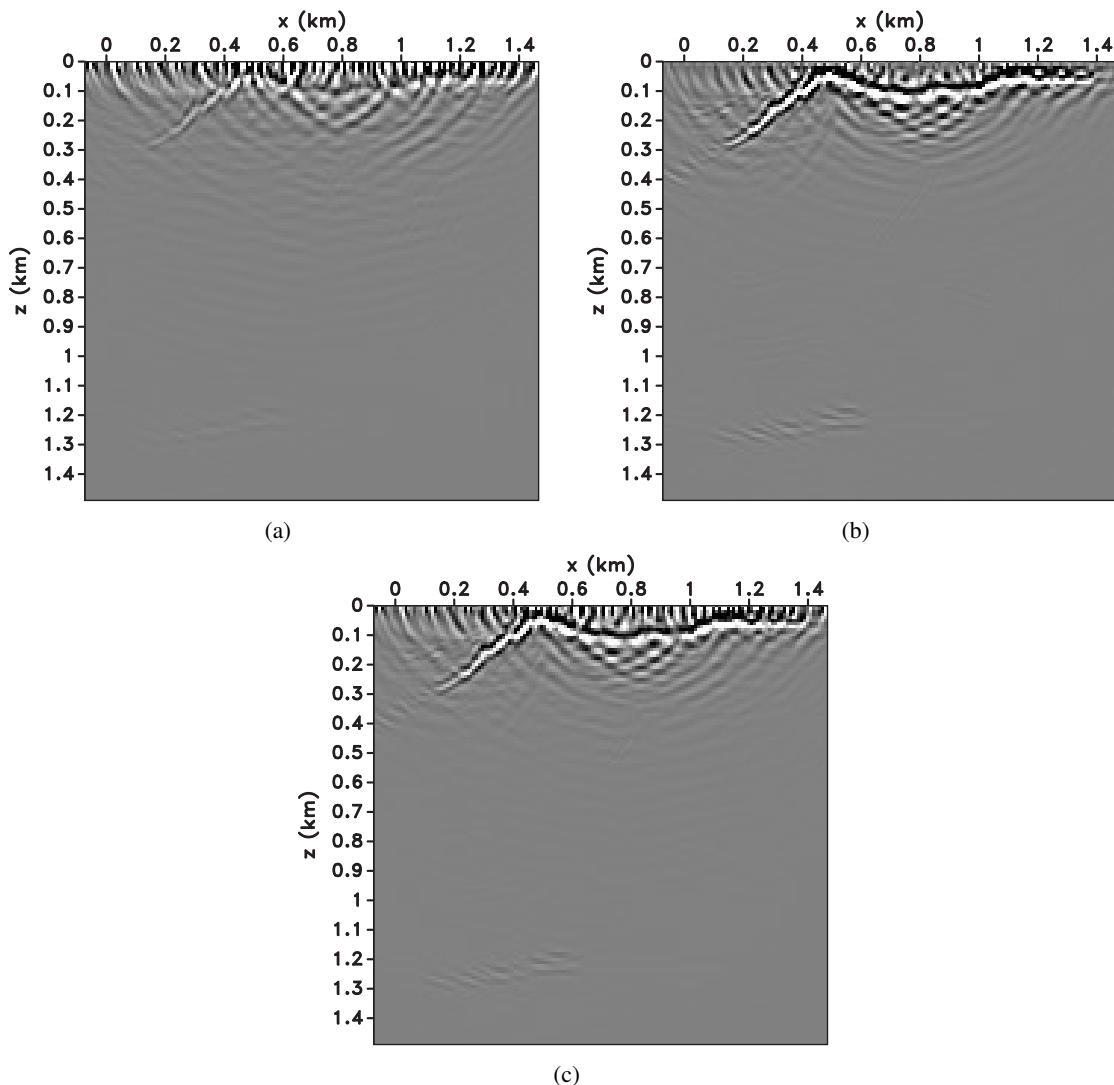


Figure 6: (a) Resulting image from migrating geophone synthetic data. (b) Resulting image from migrating DAS synthetic data. (c) Combined image from migrating DAS and geophone synthetic data.

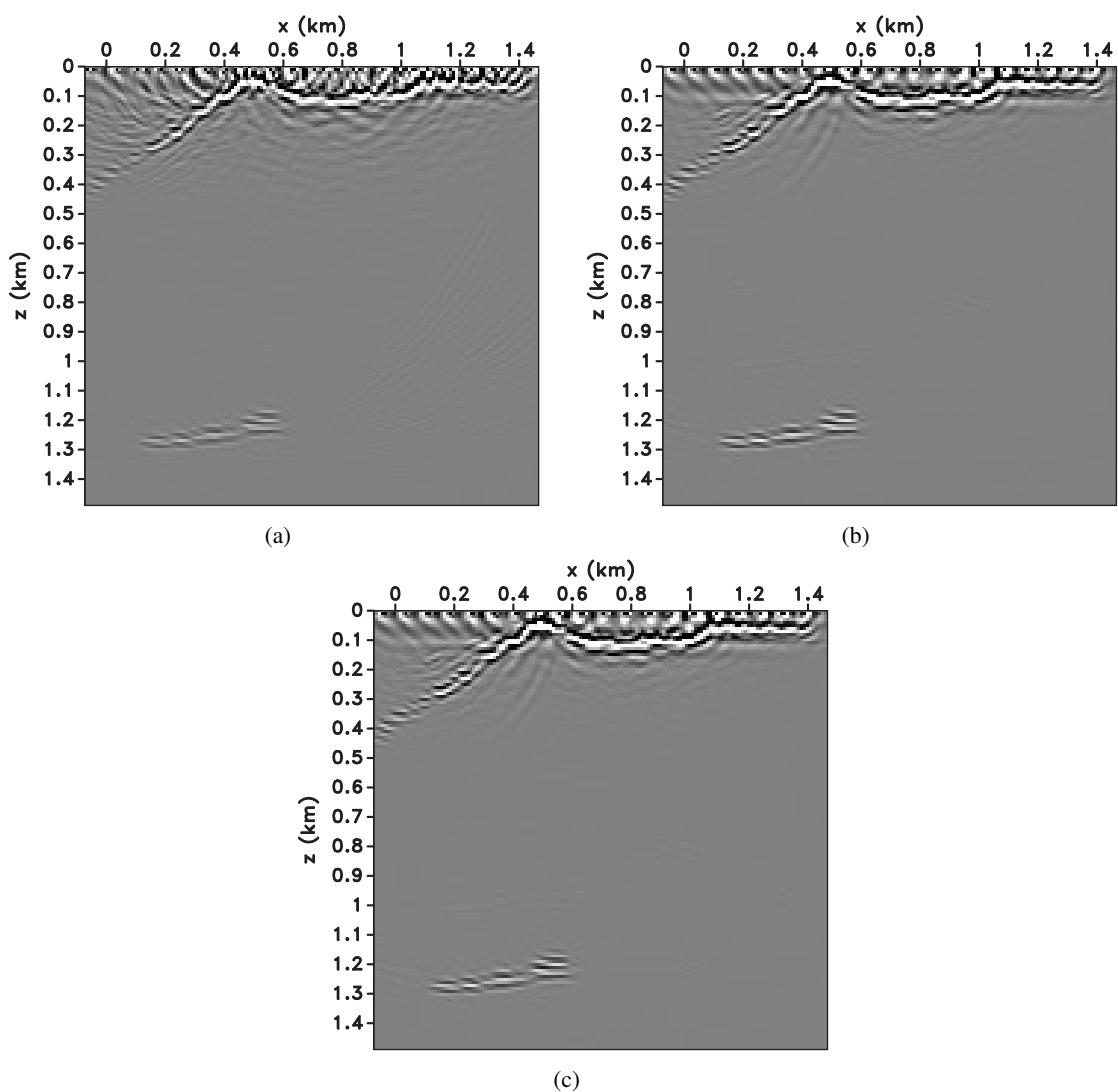


Figure 7: (a) Resulting image from migrating geophone synthetic data. (b) Resulting image from migrating DAS synthetic data. (c) Combined image from migrating DAS and geophone synthetic data.

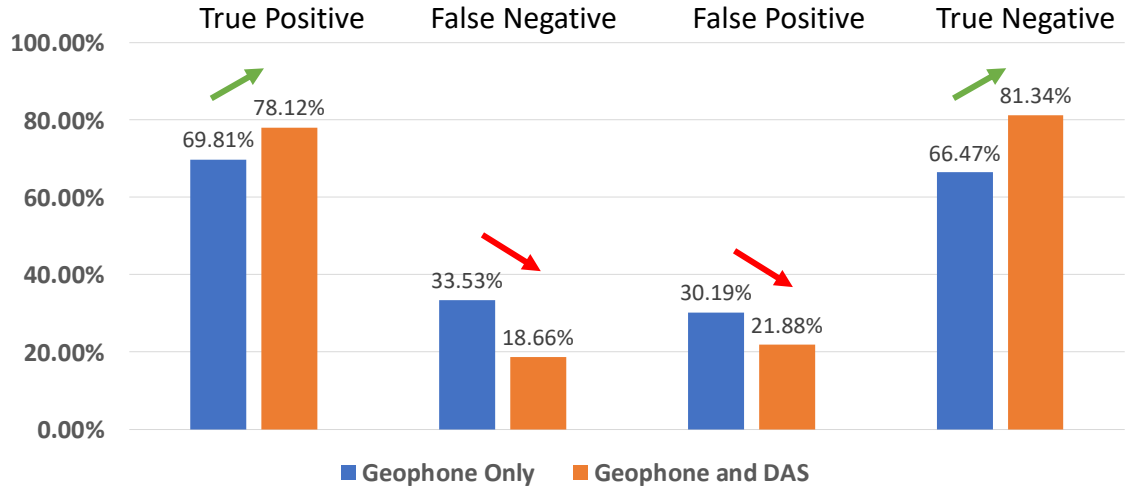


(a)

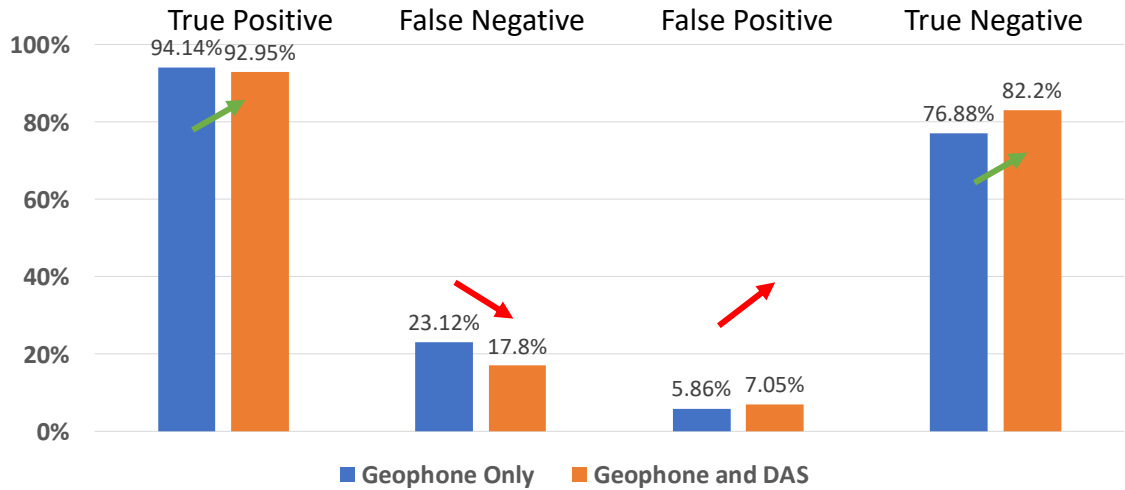


(b)

Figure 8: (a) Examples of the automatically generated faults images used to train the CNN. (b) Examples of the automatically generated images that were not faults used to train the CNN.



(a)



(b)

Figure 9: Posterior reliability of information from CNN's calculated using Equation 3 using (a) a vertical force and (b) a horizontal force. The objective is to maximize the percentages of true positives and negatives (green arrows) while minimizing the percentages of false positives and negatives (red arrows). This is obtained by having better instruments as well as better classification.

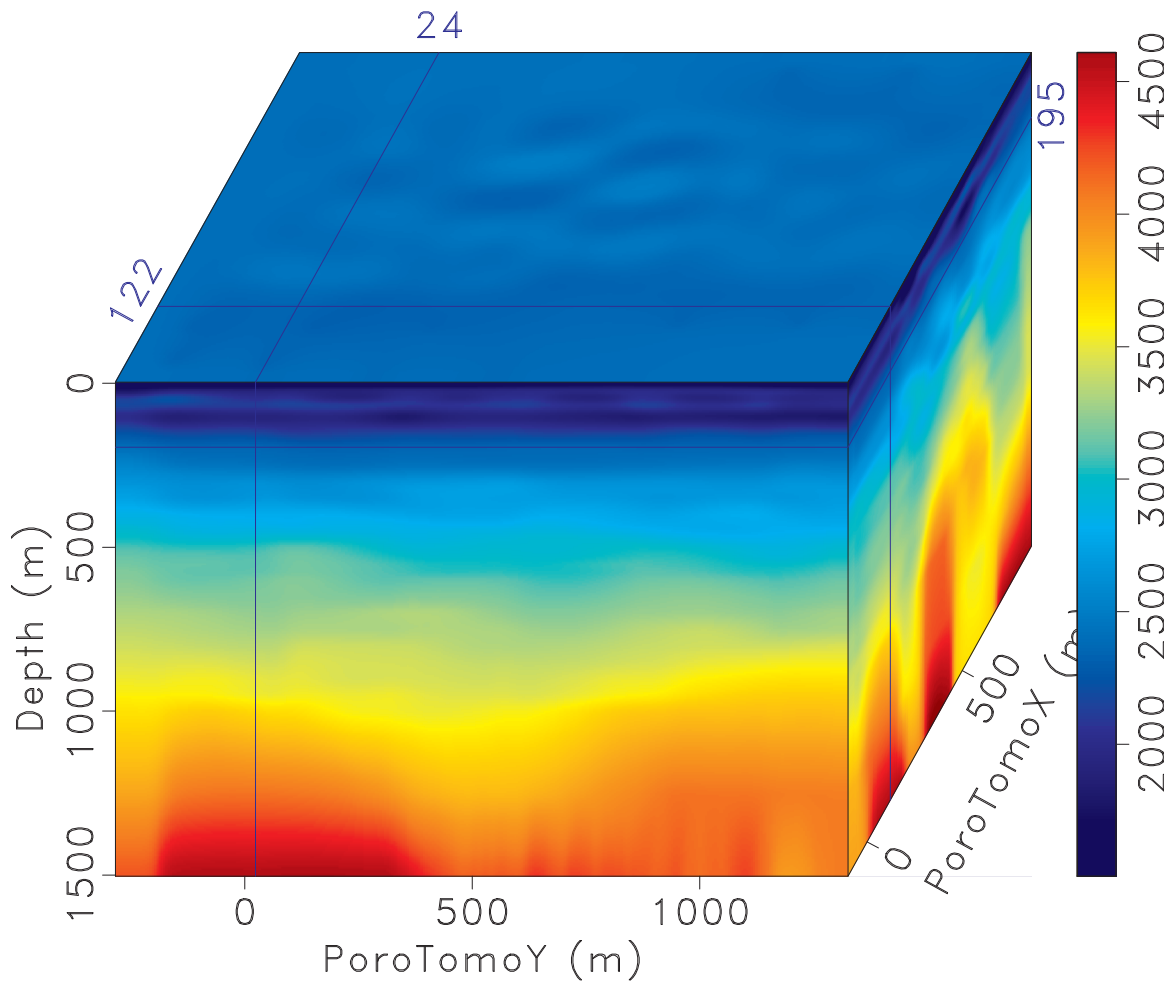


Figure 10: Body wave (P-wave) velocity (m/s) model from sweep interferometry in 3D perspective (Matzel et al., 2017b).

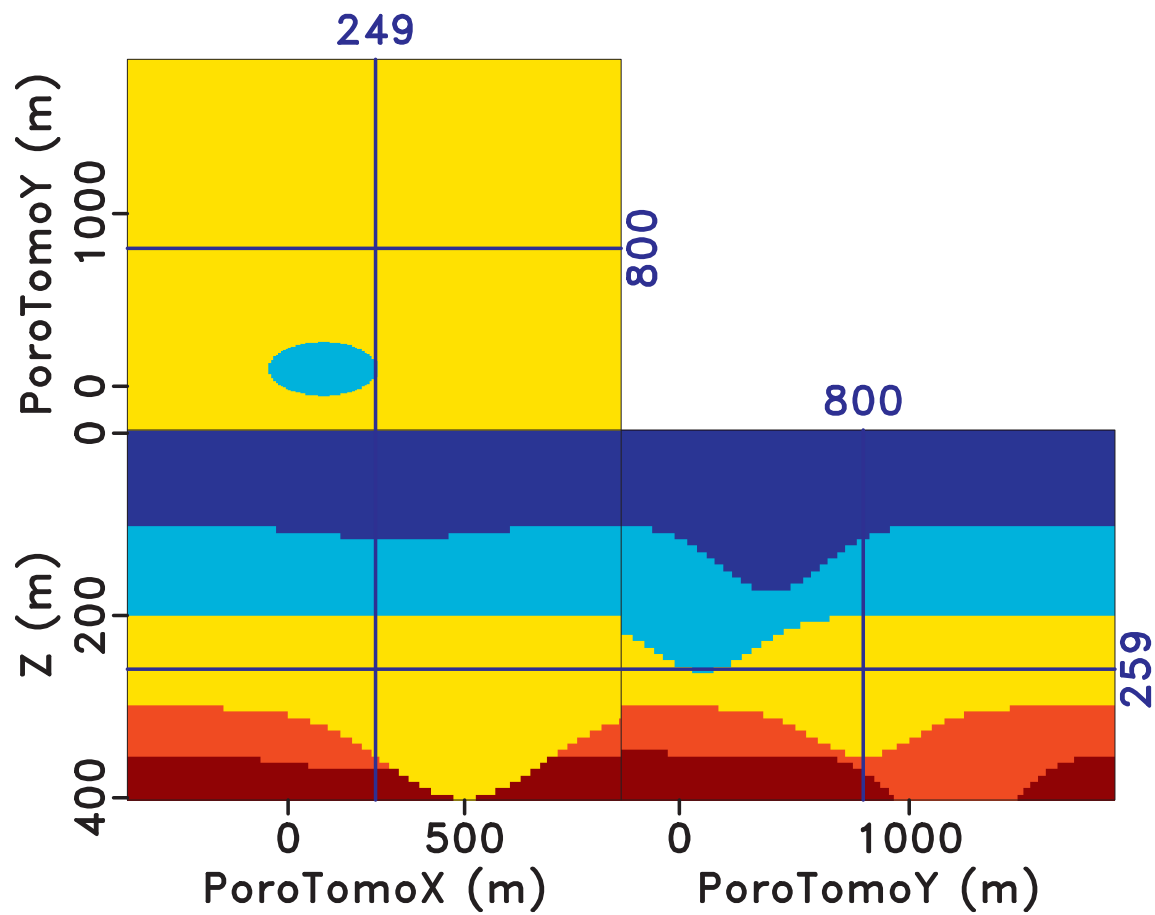


Figure 11: Four layer model with a variety of structures used for data modeling. This model is used as a density model for elastic modeling.

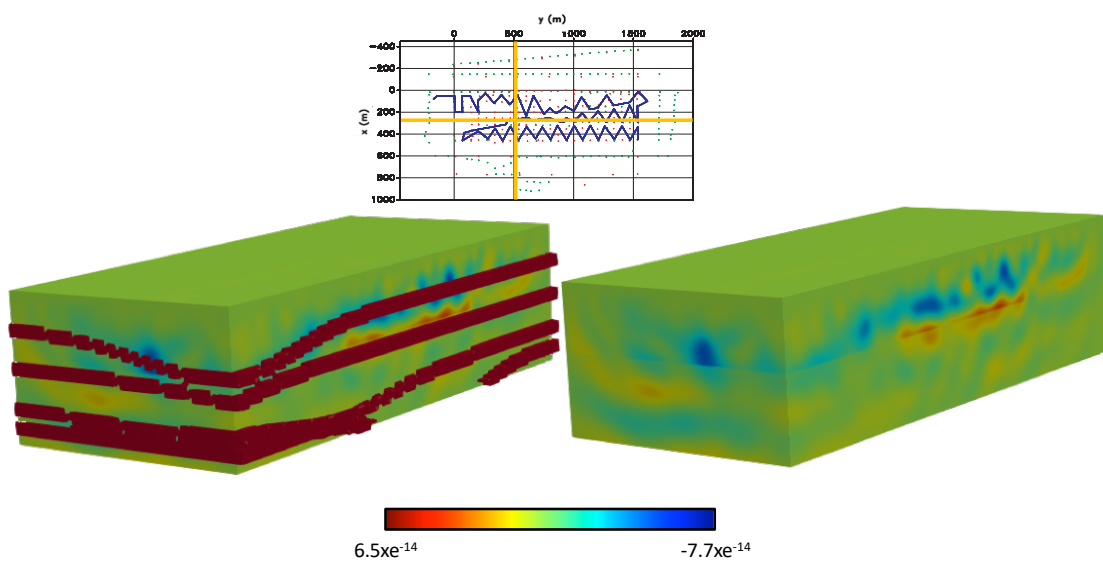


Figure 12: Results of migrating the reflectivity model (Figure 11) using the PoroTomo DAS acquisition shown on the right. The true reflectivity model is overlain and shown on the left. The slices on each side are taken at the yellow cross shown on the map view of the acquisition.

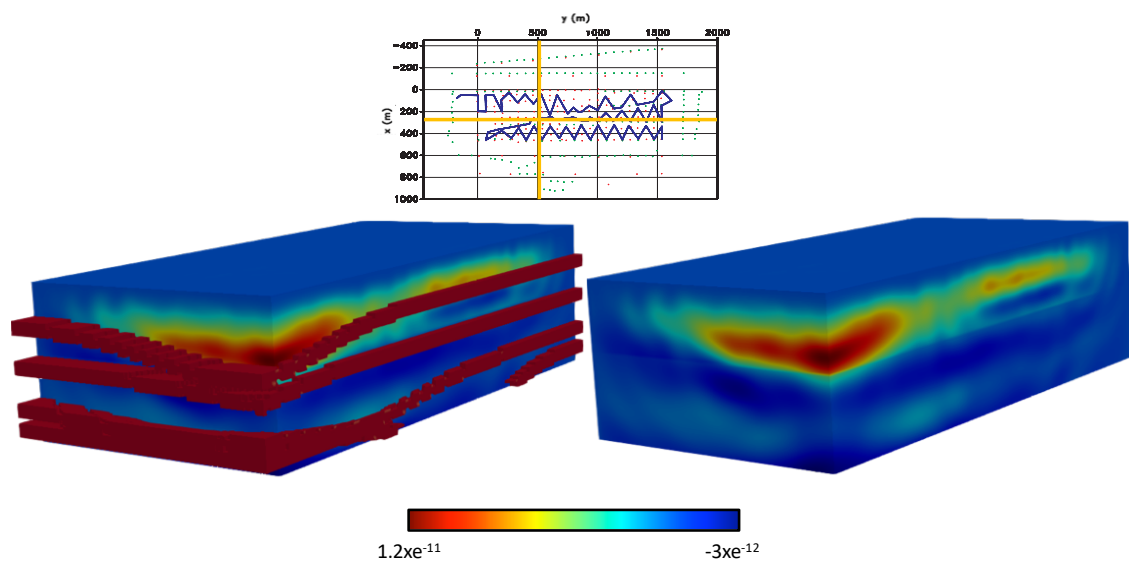


Figure 13: Results of migrating the reflectivity model (Figure 11) using the PoroTomo geophone acquisition shown on the right. The true reflectivity model is overlain and shown on the left. The slices on each side are taken at the yellow cross shown on the map view of the acquisition.

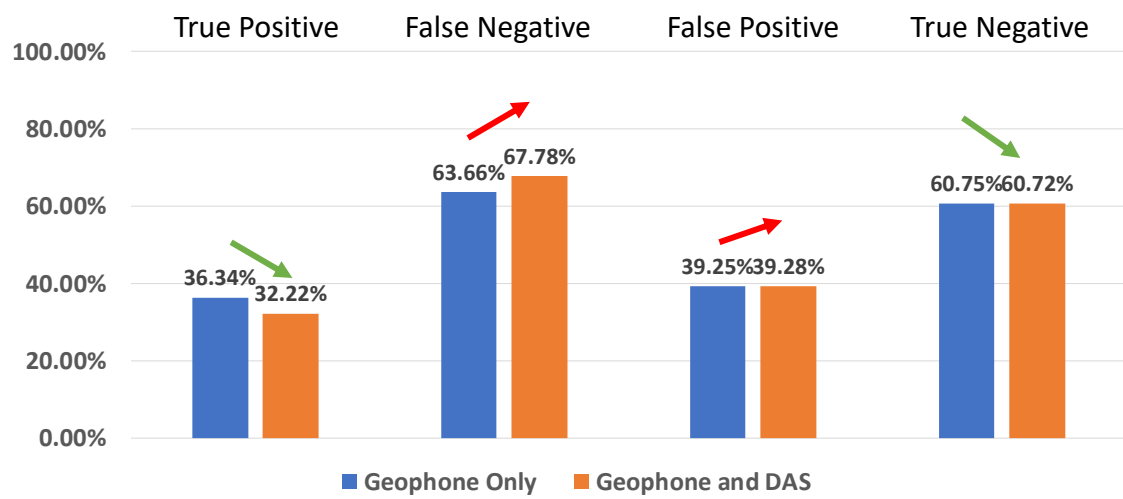


Figure 14: Posterior reliability of information from energy norm filtering calculated using Equation 3 using a horizontal force. The objective is to maximize the percentages of true positives and negatives (green arrows) while minimizing the percentages of false positives and negatives (red arrows).

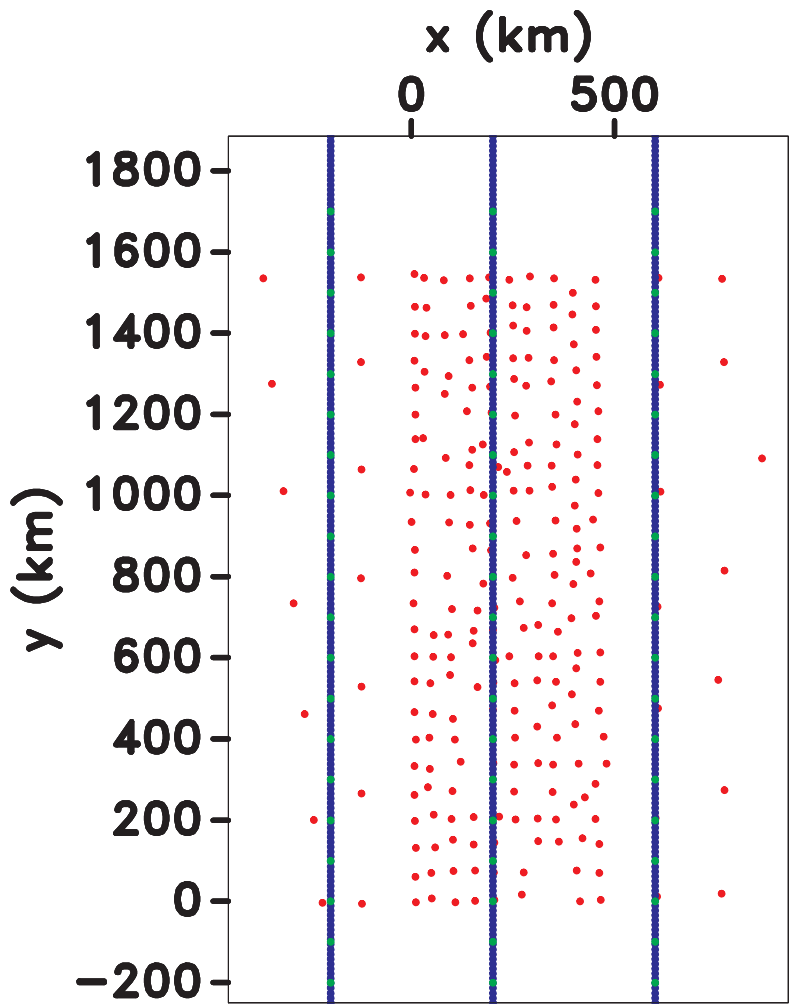


Figure 15: New survey geometry proposed to test the effectiveness of surface DAS fiber. Green dots represent source locations, red dots represent geophone locations, and the blue lines represent the surface DAS acquisition.

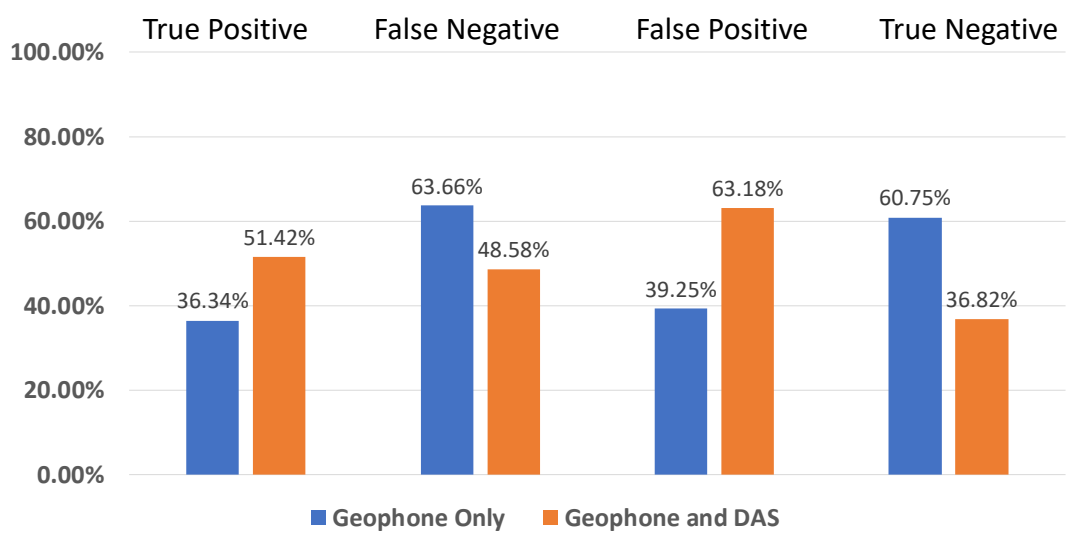


Figure 16: Posterior reliability of information using a horizontal force and the Figure 15 acquisition geometry.